

First-principles investigations of the magnetic phase diagram of $\text{Gd}_{1-x}\text{Ca}_x\text{MnO}_3$

Hichem Ben Hamed,^{1,*} Martin Hoffmann,^{2,†} Waheed A. Adeagbo,¹ Arthur Ernst,^{2,3}
Wolfram Hergert,¹ Teemu Hynninen,⁴ Kalevi Kokko,^{5,6} and Petriina Paturi⁴

¹*Institute of Physics, Martin Luther University Halle-Wittenberg, Von-Seckendorff-Platz 1, 06120 Halle, Germany*

²*Institute for Theoretical Physics, Johannes Kepler University Linz, Altenberger Straße 69, 4040 Linz, Austria*

³*Max Planck Institute of Microstructure Physics, Weinberg 2, 06120 Halle, Germany*

⁴*Wihuri Physical Laboratory, Department of Physics and Astronomy, University of Turku, FI-20014 Turku, Finland*

⁵*Department of Physics and Astronomy, University of Turku, FIN-20014 Turku, Finland*

⁶*Turku University Centre for Materials and Surfaces (MatSurf), Turku, Finland*

(Dated: July 13, 2022)

We studied for the first time the magnetic phase diagram of the rare-earth manganites series $\text{Gd}_{1-x}\text{Ca}_x\text{MnO}_3$ (GCMO) over the full concentration range based on density functional theory. GCMO forms a solid solution and we take into account its disorder by adapting special quasi random structures at different concentration steps. The magnetic phase diagram is mainly described by means of the magnetic exchange interactions between the Mn sites and Monte Carlo simulations were performed to estimate the corresponding transition temperatures. They agree very well with recent experiments. The hole doped region $x < 0.5$ shows a strong ferromagnetic ground state, which competes with A-type antiferromagnetism at higher Ca concentrations $x > 0.6$.

I. INTRODUCTION

Transition metal oxides are of current interest and constitute one class of promising materials to spawn diverse semiconductor devices [1]. They exhibit a wide range of exotic properties, owing mainly to the partly filled d shell [2]. The hybridization between oxygen p states and the strongly correlated $3d$ states induce intriguing spin, charge and orbital ordering. These properties are stimulated by the close interplay of structural, electronic and magnetic degrees of freedom. The discovery of the colossal magneto resistance (CMR) effect [3, 4] has triggered an intensive study of the series of rare-earth manganese oxides with general formula RMnO_3 (with variable $R = \text{La}, \text{Ce}, \dots$).

The RMnO_3 series consists of insulating perovskites, which show a multitude of antiferromagnetic (AFM) structures earlier studied by Kimura *et al.* [5]. The observed A-type AFM (A-AFM) ground state was associated with the tilting of the MnO_6 octahedron, known as GdFeO_3 -type distortion. This kind of distortion becomes even more pronounced for smaller ionic radius of the rare-earth ions (r_R).

Due to the perovskite structure of RMnO_3 , the resulting crystal-field breaks the degeneracy of the Mn^{3+} d orbitals. Thus, they split into two degenerated orbitals (e_g) and three degenerated orbitals (t_{2g}). The strong Hund's coupling favors the parallel alignment of the four electrons in the majority spin channel. The cooperative Jahn-Teller (JT) distortions lift in addition the double degeneracy of the e_g orbitals, while the t_{2g} orbitals become localized. The electrons occupying the e_g orbitals can in turn hop between the Mn sites through the p orbitals of oxygen. This mechanism is known as the double

exchange interaction mechanism and was earlier introduced in the works of Zener [6] and Anderson [7].

Recently, a special focus on RMnO_3 was raised because additional features can be accessed by modulating the electrical charge carrier density. That can be realized, e.g., with applying an electrostatic field [8] or chemical doping by introducing alkaline earth elements (abbreviated as A) at the R site.

The incorporation of alkaline earth elements is the method we want to focus on in this work because the RMnO_3 perovskite structure is very robust against adding other ions. It is already widely used since the early works of Wollan and Koehler [9] and Goodenough [10]. Several material systems were already investigated and show full miscibility between the R and A elements, e.g., the $\text{La}_{1-x}\text{Ca}_x\text{MnO}_3$ series (LCMO) [9, 10], or the $\text{Pr}_{1-x}\text{Ca}_x\text{MnO}_3$ series (PCMO) [11]. In these solid solutions, the substitution of R ions by A ions causes the Mn e_g electrons to hop to the neighboring ions – a four-valent Mn ion appears. Consequently, two types of manganese emerge in the cell, namely, Mn^{3+} and Mn^{4+} , and such systems are called mixed valence manganites.

A prominent member of the RMnO_3 series is GdMnO_3 . The main reason is its location in the magnetoelectric phase diagram of the RMnO_3 compounds as a function of r_R : in close vicinity of the collinear A-type AFM phase but also close to a ferroelectric state [13, 14]. Hence, the phases could be manipulated rather easily by external means. Kimura *et al.* [13] found, for instance, that a magnetic field of about 1 T is sufficient to produce ferroelectricity. On the other hand, GdMnO_3 could be also an important candidate for future magneto-optic devices because of its strong magneto-dielectric coupling [15].

Beiranvand *et al.* [16] studied the magnetic phase diagram of the $\text{Gd}_{1-x}\text{Ca}_x\text{MnO}_3$ series (GCMO) using magnetoresistive measurements in order to understand basic properties of this system. They reported a rich and complicated magnetic phase diagram where the CMR effect

* hichem.ben-hamed@physik.uni-halle.de

† martin.hoffmann@jku.at

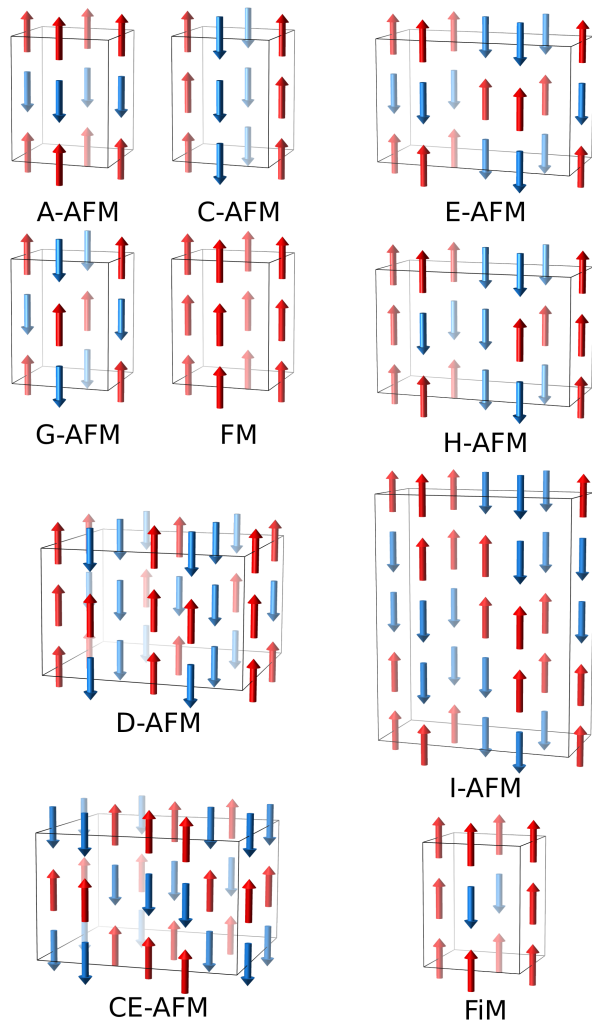


FIG. 1. The different magnetic ground state structures which were suggested in [9] and were taken into account in this work. Here, only the magnetic moments at the Mn sites are represented as arrows – red for the majority and blue for the minority spin direction. Different numbers of repeated Pbnm unit cells (see Fig. 2) are needed to depict the antiferromagnetic (AFM) structures. The opacity of the arrows has no particular meaning but only serves the perspective view. Structural figures were prepared with VESTA [12].

was observed in GCMO for doping concentrations between $x = 0.8$ and $x = 0.9$. The ferromagnetic insulating phase (FMI) in the region $x < 0.5$ transforms for $x > 0.5$ to an AFMI phase. The charge ordering state starts from $x = 0.5$, reaches its maximum at temperatures close to the room temperature, and persists until $x = 0.7$. Unlike many doped manganites, there is no indication of a metal-insulator transition below the experimental limit of 9 T.

Nevertheless, the underlying microscopic mechanisms are not yet fully understood: The entire character of the magnetic phases is unknown, because Gd and related compounds cannot be easily investigated by means of

Neutron diffraction. In fact, Gd has shown to be the strongest neutron-absorbent among all natural elements [17].

At this point, our theoretical study allows to identify the magnetic ground state by total energy calculations for various potential magnetic phases (see Fig. 1). We reexamine at first the two undoped systems GdMnO_3 (GMO) and CaMnO_3 (CMO) as a benchmark for our density functional (DFT) calculations. When going to different concentrations of the solid solution GCMO, the disorder complicates the supercell calculations, necessary to cover all magnetic structures given in Fig. 1. For that reason, we made use of the concept of special quasi random structures (SQS) for the rare-earth site mixed with Ca. The SQS method is an elegant way to model disordered systems pioneered by Zunger *et al.* [18]. The magnetic properties are discussed in terms of magnetic exchange interactions between the Mn sites. They are then used in a classical Heisenberg model in order to determine the critical magnetic transition temperature, which agrees very well with the experimental results [16]. As the main result, we derive the type of magnetic ground states, which could not be accessed directly from the magnetoresistance experiments in [16].

II. UNDOPED MANGANITES

A lot of work has already been carried out on the theoretical description of both endpoint compounds in the GCMO series. We refer the reader for more details to [19–24] for GdMnO_3 and [25–30] for CaMnO_3 . We aim at the beginning to validate the structural, electronic and magnetic properties against the previous theoretical and experimental results as a benchmark for the following discussion of the phase diagram in section III.

Our density functional theory (DFT) calculations were carried out with the projector augmented-wave method [31] as implemented in the Vienna *ab initio* simulation package (VASP) [32, 33]. For the treatment of the exchange correlation potential, we considered four common functionals: Perdew-Burke-Ernzerhof (PBE) [34], its revised version for solids (PBEsol) [34], Perdew-Wang (PW91) [35], and Perdew-Zunger (PZ) [36]. An isotropic screened on-site Coulomb interaction [37] is added to all aforementioned functionals. The choice of the Hubbard U correction and the exchange correlation functional was made based on the best compromise between the three most important properties: the electronic band gap, the magnetic moment, and primarily the stability of the magnetic order. From those properties, we considered PBE+ U with $U_{\text{Mn}} = 2 \text{ eV}$ for the Mn $3d$ orbitals as the best choice. A thoroughly discussion and comparison is given in the supplemental material [38].

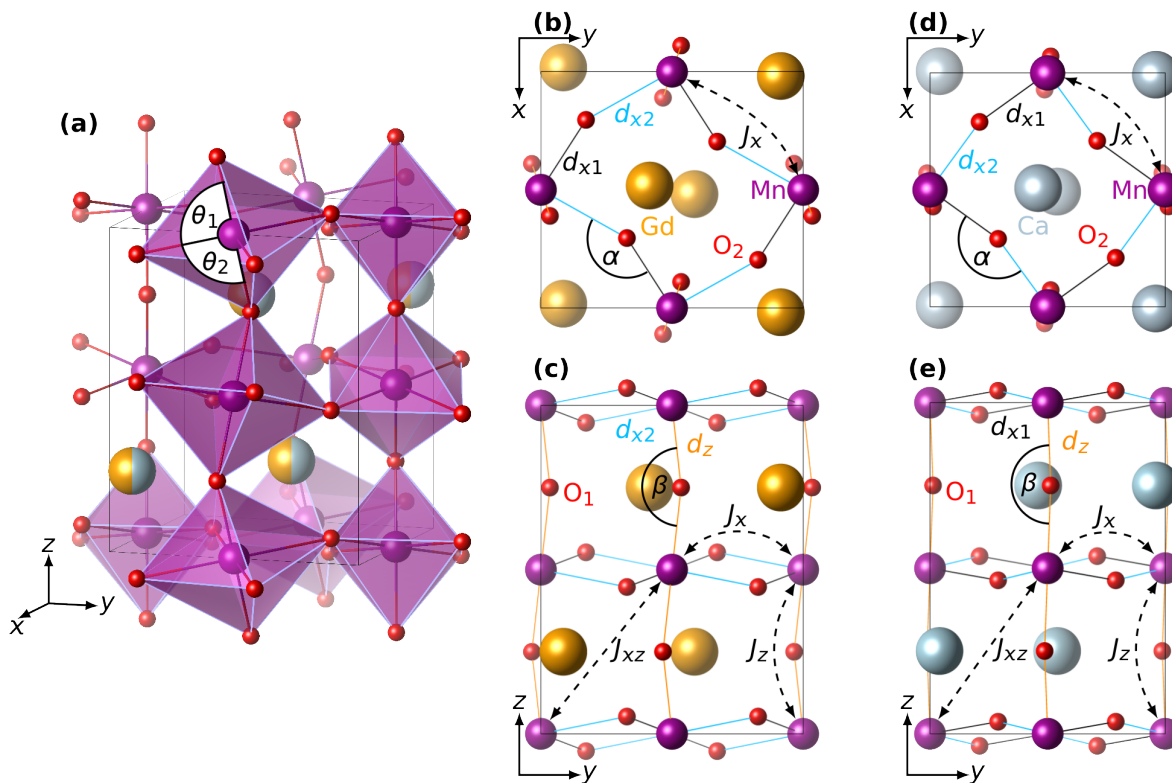


FIG. 2. Structural representation of the $Pbnm$ unit cell of GCMO. (a) Schematic of the 3-dimensional unit cell including the distorted oxygen octahedra. (b),(c) $GdMnO_3$ and (d),(e) $CaMnO_3$. The colored balls depict the R site (mixed colors), Gd (golden), Ca (gray), Mn (violet), and oxygen (red). (b),(d) show the respective top view (xy plane). (c),(e) feature the side view (yz plane). The structural notation is also indicated for bond length Mn–O and the bond angle enclosed in the Mn–O–Mn bond (α and β). The three different bond length are noted as (Mn–O) $_z$ (orange, d_z), (Mn–O) $_{x1}$ (black, d_{x1}), and (Mn–O) $_{x2}$ (blue, d_{x2}). The direction of the magnetic exchange interactions between the Mn sites is pictured as well with dashed arrows. The θ_i in (a) represent two of the eight intra-octahedron bond angles. Structural figures were prepared with VESTA [12].

A. Lattice Structure

Both compounds crystallize in the orthorhombic structure with the $Pbnm$ symmetry of the space group 62 including 20 sites (Fig. 2). The Gd or Ca atoms occupy the $4c$ Wyckoff position $(x_R, y_R, 1/4)$, while the Mn atoms are at the $4b$ Wyckoff position $(1/2, 0, 0)$. The oxygen atoms are located at two different sites and are denoted as O_1 for $4c$ $(x_{O_1}, y_{O_1}, 1/4)$ and $8d$ $(x_{O_2}, y_{O_2}, z_{O_2})$ (see Table I). The first type of oxygen ions (O_1) forms bonds with the Mn in z direction, while the second type (O_2) is bonded to Mn ions in the (xy) plane (see Fig. 2).

We considered two different lattice relaxations in order to obtain the GMO and CMO ground state structures. On one hand, we fixed the lattice parameters and the volume to the experimental volume measured in [16] and relaxed only the internal coordinates. It is referred as V_0 in Table I. On the other hand, we did a full relaxation of the structures – referred as V_{rlx} in Table I.

Both relaxation modes show the characteristic magnetite lattice distortions as described in the introduction. The deviations from the ideal cubic perovskite can

be quantified using the two angles, α and β (Fig. 2), the Baur’s distortion index (B_D) [41], and the bond angle variance (σ^2) [42]. B_D expresses the deviations of the Mn–O distances from their mean value. In an undistorted octahedron, the three Mn–O distances are equivalent and B_D is zero. The bond angle variance measures the distortion of intra-octahedron bond angles θ_i from its ideal counterpart octahedron with the same volume. With no distortion, σ^2 becomes as well zero, because the θ_i are 90° . The two former indices measure the intra-octahedron distortions while both angles α and β quantify the collective octahedral tilting (Fig. 2).

The full relaxation (V_{rlx}) of GMO volume leads to an overestimation by about 1.6% compared to experimental values (Table I). Consecutively, the octahedron volume was found to be 3% larger than in Refs. [16, 39]. As well, the relaxed CMO structure and its octahedron volume were found to be overestimated by 1.8% and 2%, respectively. Such overestimation is known as a characteristic of the GGA functionals in general.

On the other hand, when we take the experimental lattice constants of [16] (V_0), the internal coordinates

TABLE I. Experimental and calculated structural properties of GMO and CMO. The lattice constants (a , b , and c) and the bond lengths d_z , d_{x1} and d_{x2} are given in Å. The latter correspond to $(\text{Mn-O})_z$, $(\text{Mn-O})_{x1}$ and $(\text{Mn-O})_{x2}$, respectively (see Fig. 2). the Baur’s distortion index B_D is dimensionless. The angle variance σ^2 is in degree². The Wyckoff positions are given in units of the lattice vectors.

	GdMnO ₃				CaMnO ₃			
	Exp		DFT		Exp		DFT	
	[39]	[16]	V_0	V_{rlx}	[40]	[16]	V_0	V_{rlx}
a	5.318	5.309	5.309	5.344	5.270	5.269	5.269	5.294
b	5.866	5.852	5.852	5.937	5.289	5.269	5.269	5.332
c	7.431	7.425	7.425	7.426	7.456	7.459	7.459	7.496
x_R	0.938	0.983	0.981	0.981	0.996	0.989	0.992	0.992
y_R	0.080	0.079	0.082	0.085	0.019	0.038	0.040	0.040
x_{O_1}	0.103	0.106	0.109	0.110	0.065	0.045	0.074	0.071
y_{O_1}	0.471	0.464	0.465	0.465	0.493	0.489	0.486	0.487
x_{O_2}	0.205	0.211	0.203	0.204	0.208	0.215	0.208	0.209
y_{O_2}	0.175	0.180	0.175	0.172	0.212	0.187	0.290	0.210
z_{O_2}	0.550	0.554	0.552	0.552	0.536	0.536	0.538	0.536
d_z	1.944	1.950	1.958	1.958	1.896	1.881	1.906	1.912
d_{x1}	1.910	1.904	1.920	1.923	1.897	1.816	1.909	1.920
d_{x2}	2.228	2.21	2.224	2.265	2.228	2.021	1.913	1.923
B_D	0.065	0.063	0.062	0.070	0.0056	0.040	0.001	0.002
σ^2	3.883	5.972	5.915	6.776	0.666	7.063	0.457	0.218

vary only slightly from both experimental and volume-relaxed structures (Table I). The resulting Mn–O bond lengths are in good agreement with those in [16, 39]. We conclude that the structural originated Jahn-Teller distortion in GMO compared to [16, 39] is well reproduced by our DFT calculation considering the two distortions indices and the relaxed coordinates (Table I).

The two experimental structures of CMO (Table I) differ considerably unlike those for GMO, especially at the y_{O_2} coordinate. This difference is demonstrated by the large B_D in [16] compared to [40] (one order of magnitude). Using the structure in [16] as a starting point for the V_0 relaxation scheme leads to a larger value of y_{O_2} than that of [40]. Only the full relaxation scheme gives a good agreement with the coordinate reported in [40]. The same statements applies here to the distortions indices, B_D and σ^2 . Overall, our calculated V_0 structure is in reasonable agreement with [40] in terms of crystal coordinates and the octahedral distortion indices. The lowering of the octahedron distortion is well manifested in all studied CMO structures compared to GMO. The three Mn–O bond lengths do not differ much contrarily to what was shown for GMO.

Our structural studies have demonstrated the importance of atomic relaxations especially for CMO. To avoid

any problems arising from the PBE’s overestimation or possible deviations in the experimental coordinates, we adapt hereafter for our structural setup the theoretical relaxed coordinates inside the reported experimental cells [16].

Considering the electronic structure, we obtained an insulating state for both compounds – GMO and CMO. Our calculated Kohn-Sham band gap of GMO without correlation corrections (0.38 eV) agreed with the result by Kováčik *et al.* [19]. It increases to 1.1 eV with our choice of $U = 2$ eV [38], although it is still below experimental band gaps obtained from UV absorption spectra of GMO nanoparticles (2.0 eV) [43] or optical measurements (2.9 eV) [44]. We observe a strong hybridization between e_g states and O p states at the valence band maximum of the A-AFM ground state of GMO (see discussion of magnetic ground states below), while the conduction band minimum is formed by a notable mixing between Mn e_g and t_{2g} states. The e_g -like valence band width is 0.95 eV, in line with the reported GW band structure [19].

We obtain similar features for the calculated band gap of CMO obtained with PBE+ U , which is 0.92 eV. This value is again lower than the experimental band gap (1.55 eV) measured for single crystals of CMO [45].

B. Mapping to a classical Heisenberg model and determination of transition temperatures

The Gd³⁺ ion has the largest magnetic moment of all the rare-earth elements caused by 7 unpaired spins. The Gd spins in GdMnO₃ show the largest observed ordering temperature (6.5 K [46]) of rare-earth elements in $RMnO_3$. Hence, the Gd-Gd interaction is negligible against the magnetic interaction between the Mn ions and the magnetic phase transition could be described in accordance with the Mn $3d$ - $3d$ and Mn-Gd $3d$ - $4f$ interactions. Owing to the complexity which arises from considering the $3d$ - $4f$ interplay, we restrict ourselves to the magnetic ordering of the the Mn ions. The f -electrons are treated as frozen in the core region. Consequently, when we speak in the following about a magnetic order, we only refer to the orientation of the Mn magnetic moments.

In order to identify the magnetic ground state structures, we needed a large common supercell to accommodate all possible magnetic configurations shown in Fig. 1. The different ferromagnetic (FM), ferrimagnetic (FiM), and antiferromagnetic structures (A-type, G-type, ... AFM) are illustrated in their minimal required cell in Fig. 1. Hence, the primitive Pbnm cell is repeated $2 \times 2 \times 2$ times resulting in supercells of 160 sites. The cell parameters were as well fixed to the experimental values [16] and the internal coordinates were relaxed in the FM spin configuration. Afterwards, the total energies are calculated within this fixed structure for different Mn spin orientations. Those magnetic struc-

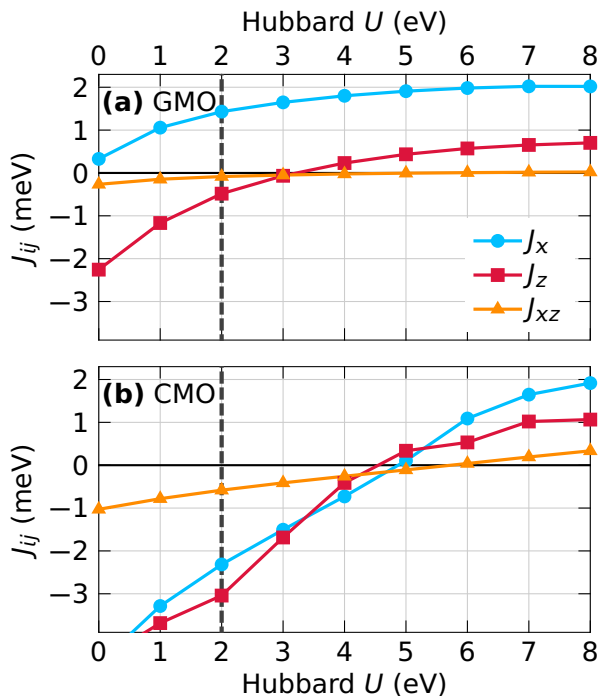


FIG. 3. The three Heisenberg exchange interactions in dependence of the correlation treatment in (a) GdMnO₃ and (b) CaMnO₃. The gray dashed line indicates the choice of $U = 2$ eV in this work. See Fig. 2 for the visualization of the three magnetic coupling directions.

tures with the lowest total energy resemble the magnetic ground state. We stay with the fixed structure due to the large cell size and primarily because we did not find any qualitative changes in the total energy differences for the respective magnetic structures when using the structure obtained by relaxing with the A-AFM spin configuration.

The relative total energies can then be used to verify the experimentally found ground states [5, 40]. We identified the A-AFM and G-AFM as those magnetic structures with the lowest total energy for GMO and CMO, respectively [38]. However, those ground states are not very stable against magnetic variations, since in both cases other magnetic structures are close in energy (FM for GMO, C-AFM for CMO) (see also Fig. 6a).

As mentioned above in the introduction, the Mn ion appears in two different valence states for GMO (Mn³⁺) and CMO (Mn⁴⁺) due to the different valence electron configuration of Gd and Ca. We obtain from our DFT calculations magnetic moments of $3.6\mu_B$ for Mn³⁺ (GMO) and $2.7\mu_B$ for Mn⁴⁺ (CMO), which substantially deviate from their integral value of $4\mu_B$ and $3\mu_B$, respectively. In GMO, this deviation is caused by the aforementioned hybridization of the Mn states with the oxygen states introducing also a magnetic moment of $0.06\mu_B$ at the oxygen ions. Our observed local magnetic moment of CMO is in line with its experimental value of $2.665\mu_B$ [9], while we did not find any experimental value of the local magnetic moment of Mn³⁺ in GMO. Nevertheless,

the $3.6\mu_B$ for Mn³⁺ in GMO agree with earlier numerical calculations including hybrid functionals [19].

In addition to the magnetic ground state, we will need below for a full description of the magnetic phase diagram of GCMO also the corresponding finite temperature characteristics – namely the critical transition temperatures. The latter can be derived on basis of the classical Heisenberg model from DFT total energies. Therefore, the total energies are mapped onto a Hamiltonian of the form

$$\hat{H} = -\frac{1}{2} \left(J_x \sum_{i \neq j} \mathbf{S}_i \cdot \mathbf{S}_j + J_z \sum_{i \neq j} \mathbf{S}_i \cdot \mathbf{S}_j + J_{xz} \sum_{i \neq j} \mathbf{S}_i \cdot \mathbf{S}_j \right), \quad (1)$$

which includes three magnetic exchange interactions J_{ij} between the Mn ions – all indicated in Fig. 2. J_x stands for the in-plane exchange interactions between the Mn nearest neighbors. The out-of-plane exchange interactions between the Mn nearest neighbors with main contributions along the z -axis are presented by J_z , while J_{xz} represents the exchange interactions along the cell diagonal direction (see Fig. 2). The sums in (1) run over all sites i with the interaction sites corresponding to each J_{ij} . Positive (negative) J_{ij} correspond to FM (AFM) coupling. The spin moment S in (1) equals to 2 for Mn³⁺ (4 unpaired electrons/2) and $3/2$ for Mn⁴⁺ (3 unpaired electrons/2). This kind of Hamiltonian was used to study magnetic properties of GMO before [19] and has an advantage over many other studies on magnetic properties of RMnO₃ being restricted only to the nearest Mn neighbors exchange couplings.

The three magnetic exchange parameters can be then obtained by mapping total energies of different spin orientations (Fig. 1) onto the Heisenberg Hamiltonian in (1). This results in an over-determined set of equations, which is solved with a linear least square fit. The ferromagnetic configuration FiM was used (Fig. 1) as the reference energy E_0 inspired by [19].

At this point, we want to emphasize the importance of a correct electronic correlation treatment in our materials. Our obtained magnetic exchange interactions vary strongly with increasing U parameters (Fig. 3). For GMO with plain PBE exchange correlation functional, the magnetic ground state is not A-type but wrongly G-type AFM (Fig. 3a). The out-of-plane J_z dominates over the other interactions. Only when U is increased to be around 2 eV, the in-plane interactions become stronger and leads to the known A-AFM phase. Increasing U further results in the FM structure, which is close in energy anyway [38].

For CMO, the situation is slightly different. The three exchange interactions are negative for plain PBE (see Fig. 3b) and only become positive for $U > 5$ eV, which is far above a reasonable value considering other materials properties. The strong competition between the three exchange parameters for $U < 4$ eV leads to the G-type AFM phase.

Finally, we want to assess the magnetic transition temperature (either T_N for AFM phases or T_C for FM and

FiM) and used our own Monte-Carlo code [47] together with the Heisenberg Hamiltonian (1). A large cluster with a volume of about 100 \AA^3 is considered repeating the primitive unit cell $16 \times 16 \times 16$ times and applied periodic boundary conditions. The thermal equilibrium was firstly assumed to be reached after 60 000 MC steps. Another 20 000 are then used in the thermal averaging. We started from the high temperature of 500 K and cooled down the GCMO samples in steps of 3 K. The transition temperatures are later extracted from the temperature dependence of three quantities – the magnetic susceptibility, saturation magnetization, and the heat capacity. The calculated exchange interactions are used for the initial system configuration. An ordering temperature of 42 K was obtained for GCMO, which matches perfectly the experimental value of 40 K [5, 46]. In contrast, a hybrid functional calculation led to a little overestimation of T_N by about 20 K [19]. For CMO, a T_N of 96 K was obtained, which is in the same range as the experimentally observed T_N of 125 K [48].

We conclude that our computational setup and the procedures in order to obtain the magnetic ground state and the magnetic transition temperatures produce results in good agreement with available experimental data. Therefore, we have a proper basis for the study of the complete series of intermixed rare-earth and alkaline earth manganites.

III. PHASE DIAGRAM FOR GCMO

The experimental measurements by Beiranvand *et al.* [16] show that the orthorhombic structure is stable for all Ca concentrations x in the $\text{Gd}_{1-x}\text{Ca}_x\text{MnO}_3$ series. This further validates our choice of adapting the experimental lattice constants in our calculations.

In addition, we want to take into account the disordered character of this solid solution. One possible way is to average the (Gd,Ca) sublattice occupancy over different structures within a large supercell with N functional units. Such method is impractical since one has to average 2^N configurations. In order to circumvent the problem, we used the special quasi-random structure (SQS) method [18] for the (Gd,Ca) sublattice. SQS takes into account the random nature of alloys by choosing the occupation of the internal coordinates inside a supercell in such a way that the pair and multi-site correlations mimic as much as possible those of a random substitutional alloy. The multi-site correlations in the SQS candidates are then taken into account and compared to the random distribution up to a defined cutoff radius.

To the best of our knowledge, it is the first time that the SQS method is applied to such manganites. The generation of the SQS cells was carried out using a Monte-Carlo annealing loop, as implemented in the MCSQS routine of the ATAT package [49]. We forced the axis orthogonality in the SQS cells, which kept the distance between the Mn sites and mostly the angles between them con-

strained throughout the GCMO series. In this way, we can keep the same definition of the three aforementioned exchange coupling in (II B) for the following comparison of magnetic properties throughout the concentration range.

Nevertheless, the concentration x cannot be chosen continuously between 0% to 100% but depends on the size of the supercell. We used here supercells constructed of $2 \times 2 \times 2$ the primitive unit cells (with 160 sites). Therefore, the smallest concentration step used in the simulation can be only $1/2^3 = 1/8$ and we performed all calculations for the concentrations $x = 0, 1/8, 1/4, \dots, 7/8$.

Many SQS reported in the literature are obtained only by matching just pair correlations. In this work, we include also higher order correlations of the random structure. Pair clusters are taken up to the 5th nearest neighbor, triplet and quadruplet clusters are included up to the 4th nearest neighbor. Only for $x = 0.5$, the SQS structure fully resembles a completely disordered system with zero correlation functions. The other correlation function results and structural details of the SQS are collected in the SI [38].

The coupling between spin, charge, lattice and orbital ordering becomes more complicated with doping, especially with large supercells. A careful consideration of the interplay of all mentioned degrees of freedom at the same time should be taken into account, which is far from trivial. Therefore, we restrict ourselves only to the coupling between the lattice structure, the occupation and the spins.

The experimental lattice parameter a and $c/\sqrt{2}$ vary only little with a slight maximum for $x = 0.5$. Only b decreases strongly until $x = 0.5$ and follows afterwards a and $c/\sqrt{2}$ [16]. Nevertheless, the unit cell volume of GCMO contracts within the gain of Mn^{4+} content (increasing x), which is essentially ascribed to the smaller ionic radius [50] of Mn^{4+} (0.53 Å) compared to that of Mn^{3+} (0.645 Å). Only Ca^{2+} has a larger ionic radius (1.34 Å) than Gd^{3+} (1.21 Å). This proves once again the importance of the Mn bonding in the description of the GCMO series and, hence, the variation of magnetic properties due to the crucial double exchange via Mn–O–Mn bonds.

We tracked the variation of the rotations of the Mn octahedra via the bond angles and bond lengths (Fig. 4). The changes of the bond lengths match the behavior of the experimental lattice constants with doping concentration in having distinct changes at $x = 0.5$ (Fig. 4a), which holds also true for the Mn–O–Mn bonds angles (Fig. 4b). In order to get the bond lengths (angles) of all GCMO compounds, we calculated the mean value of all present bond lengths (angles) inside the relaxed SQS cells. As well, the distortion indices (B_D and σ^2) decrease linearly with increasing x , except at $x = 5/8$ where it shows an anomaly. This follows exactly the peculiar deviation of the cell parameters with the already stated concentration.

The calculated density of states of the GCMO series

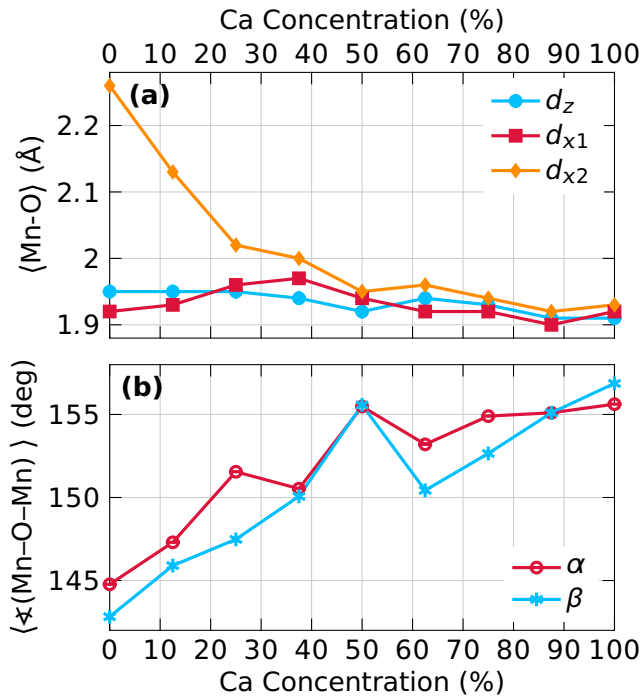


FIG. 4. The variation of (a) the three Mn–O bond lengths and (b) the Mn–O–Mn bond angles averaged over the SQS bond lengths and angles, respectively, with respect to the Ca concentration in the whole GCMO series. See Fig. 2 for the visualization of both structural properties.

shows a half-metallic-like behavior in the majority spin channel, while the minority spin gives rise to band gaps between 1 eV and 1.5 eV. A similar result was shown for $\text{La}_{1-x}\text{Ca}_x\text{MnO}_3$ [51], where the insulating character of the density of states was only recovered by localizing the additional electron (hole) in the system.

The magnetic ground state structures for GCMO are determined, as in the section II B, for the SQS at every concentration as well. The number of relevant magnetic exchange interactions remains also the same, J_x , J_z , and J_{xz} (Fig. 2), due to the conserved Mn distances in the supercells. We only vary S as the mean value of the spin moment, which corresponds to the respective Ca concentration

$$S_x = (1-x)S_{\text{Mn}^{3+}} + xS_{\text{Mn}^{4+}}, \quad (2)$$

with $S_{\text{Mn}^{3+}} = 2$ and $S_{\text{Mn}^{4+}} = 3/2$. In the case of partial occupation of Gd sublattice ($0 < x < 1$), the distinction between Mn^{3+} and Mn^{4+} is ignored in all our calculations. They are treated at the same footing as effective Mn ions with concentration dependent valence state but take a value of 3+ at $x = 0$ and 4+ in $x = 1$. Following the experimental literature [9, 10, 16], we can distinguish three different doping regimes: hole doping for $x < 1/2$, middle doping region for $1/2 \leq x < 7/8$, and electron doping $x \geq 7/8$. It is, e.g., seen in the qualitative changes of the experimental lattice constants and the Mn–O bond lengths, which show at $x = 0.5$ a turning point.

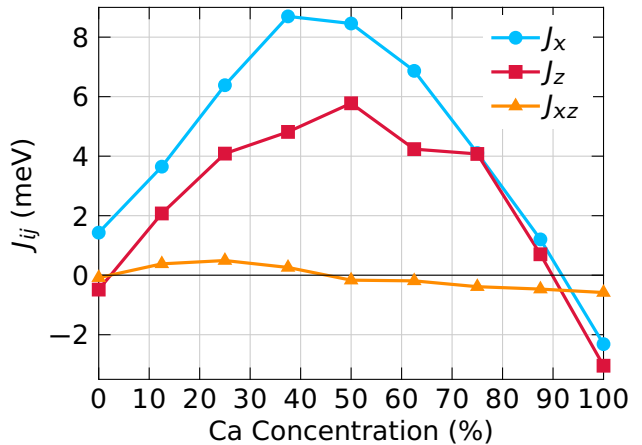


FIG. 5. The calculated Heisenberg exchange interactions in $\text{Gd}_{1-x}\text{Ca}_x\text{MnO}_3$ following equations (1) and (2). See Fig. 2 for the visualization of the three magnetic coupling directions.

A. Hole doping: $x < 1/2$

Adding Ca to GdMnO_3 introduces a hole in the vicinity of the Ca^{2+} ion, which is compensated by an additional electron from Mn – the already mentioned Mn^{4+} is created. This process causes a transition of the A-AFM phase to a FM state in the concentration range $0 < x < 0.5$, experimentally verified by Beiranvand *et al.* [16]. Their temperature dependent SQUID measurements show a negative magnetization at $x = 0.1$ and $T < 20$ K. This result stems mainly from the Gd spins, which orient antiparallel to the direction of the Mn spins. This ferrimagnetic coupling was firstly proposed for $x = 0.3$ [52] and thereafter generalized for $x < 1/2$ [16, 53] of GCMO. The same FM phase transition is obtained in our calculation with the SQS structure at $x = 1/8$. Before at $x = 0$, the FM state has not the lowest total energy but its energy difference to the A-AFM state is rather small (see Fig. 6a). The increase of the Ca concentration to $x = 1/8$ turns the sign of the total energy difference and enhances it strongly: the FM state is (29 meV) below the A-AFM state and even more for $x = 1/4$ (see Fig. 6a). This first transition is connected with a strong increase of the in-plane exchange parameter (J_x) to 3.6 eV and an AFM to FM change of the out-of-plane exchange interactions (Fig. 5). This increase in the magnetic coupling strength does not only result in the A-AFM to FM transition but also in an increased Curie temperature until $x = 1/2$ (see Fig. 6b), which qualitatively matches the experimental measurements of a FM order in the whole hole-doped region of GCMO very nicely [16, 52, 54]. Such magnetic alteration could be attributed to the progressive increase of the Mn–O–Mn bond angle with the doping level, as well as the drastic shrink of the in-plane $(\text{Mn–O})_{x2}$ bond length (Fig. 4). The Mn–O–Mn bond angle was, e.g., reported for $x = 1/4$ as 149.7° [55], which is the average of our two calculated angles, 147° and 151.7° . Accompanied with the decrease of the cell

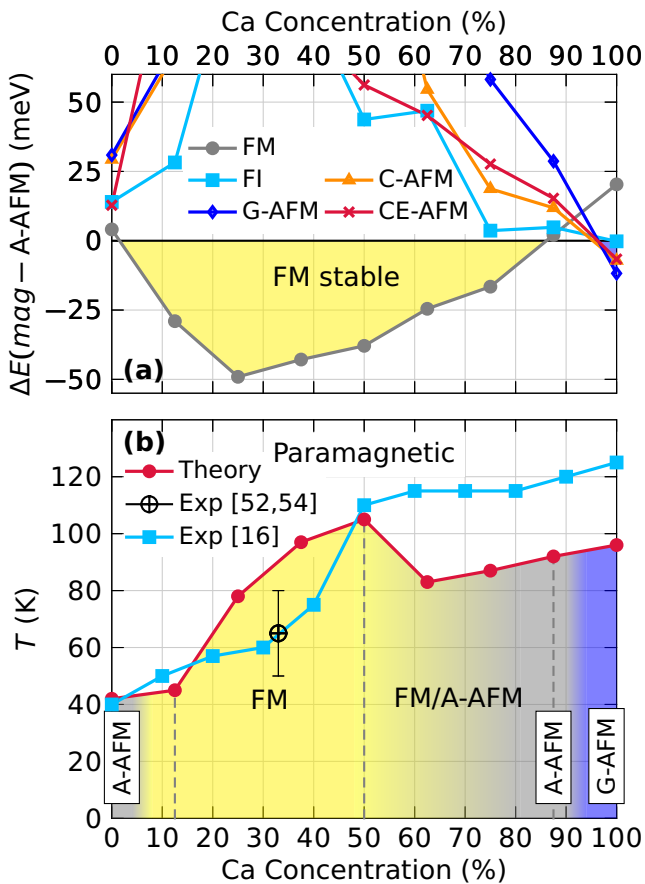


FIG. 6. (a) The concentration dependent total energy landscape of the most relevant magnetic ground state structures (*mag*) depicted in Fig. 1. The energy differences $\Delta E(\text{mag} - \text{A-AFM})$ are calculated with respect to the A-AFM state. If ΔE is negative, the respective magnetic state (*mag*) is stable. (b) The theoretical magnetic phase diagram of $\text{Gd}_{1-x}\text{Ca}_x\text{MnO}_3$. The critical temperatures (red circles) were determined via the Monte Carlo simulations, while the magnetic phases were identified from the minimal total energy. The area FM/A-AFM identifies the concentration range, where the total energy of the FM and A-AFM magnetic phase are below 25 meV. The measured critical temperatures from Ref. [16] (blue squares) and for $x = 1/3$ from Ref. [52, 54] (black \oplus with error bars) are shown for comparison. Above the critical temperature, we expect a paramagnetic state.

parameter b , the overall cell distortion diminishes and we can conclude that the Ca induced magnetic transformation is mainly triggered by the reduction of the JT distortion. The disagreement between the measured and calculated transition temperatures in Fig. 6b could have, besides the known problems of T_C calculations, several different explanations. Lattice imperfections as vacancies, in particular on the oxygen sublattice, might cause significant changes in the magnetic properties as observed for other oxides, like SrCoO_3 [56] or $\text{Sr}_2\text{FeMoO}_6$ [57]. In addition, differences can rise from the polycrystalline character of the samples in comparison with the ideal

periodic crystal from the simulation or a canted antiferromagnetic insulating state reported for $x = 0.33$ [52] than a simple ferromagnetic one.

B. Half occupied: $1/2 \leq x < 7/8$

In the mid-doped region, $x \sim 0.5$, our Monte-Carlo simulation determined a transition temperature of 105 K – close to the reported bulk temperature (107 K). And although we observed a negative J_{xz} for the first time after introducing Ca (Fig. 5), we still obtained a FM ground state structure, where the A-AFM order is the energetically closest magnetic structure (see Fig. 6).

The Mn–O–Mn angles become equivalent – both are 155° (Fig. 4b) and all Mn–O distances decrease to roughly the similar distance (Fig. 4a). Hence, the octahedron distortion becomes less pronounced than before, which hints also to the ferromagnetic order due to the double exchange mechanism following from the different valency of the Mn ions.

Nevertheless, our estimation of the magnetic ground state fails at $x \sim 0.5$ because an AFM order was reported in the experimental magnetic phase diagram [16]. The particular type of AFM order was on the one hand not accessible experimentally due to the unavailability of Neutron diffraction measurements and on the other hand accompanied with the first appearance of the charge ordering (CO) phenomenon, which remains at $x = 0.5$ thermally stable up to 270 K.

This room temperature CO state makes the mid-doped concentration range not only most interesting for technical applications but might have also an important role in the stabilization of the AFM order, which was discussed, e.g., for $\text{La}_{0.5}\text{Ca}_{0.5}\text{MnO}_3$ [58]. This compound showed a positive Curie-Weiss factor in the temperature range 275 K to 360 K, suggesting therein the dominance of the FM exchange coupling as a consequence of double exchange. But below, the AFM order stabilized due to the CO at $T < T_N$.

Another potential stabilization mechanism of the AFM order was proposed for $\text{Pr}_{1-x}\text{Ca}_x\text{MnO}_3$ (PCMO). Its magnetic order at $x = 0.5$ is rather maintained by the presence of the so called Zener polarons, because a stabilization of a CE-type AFM order by means of the CO could be excluded based on single-crystal neutron diffraction measurements [11, 59]. This phenomenon results from trapped electrons between the two Mn sites causing a valence of 3.5+ in the neighboring Mn ions instead of the natural valence of 3+ or 4+, respectively.

An analogous argument was given by García *et al.* [60] using a ferromagnetic Kondo lattice model. There-with, they demonstrate that the formation of magnetic polarons is an important ingredient in the description of systems with correlated spin-charge degree of freedoms. This correlation is induced from the strong competition between double exchange and superexchange mechanisms.

Unfortunately, these phenomena like CO or OO are very complicated to include in DFT calculations. That means a much larger computational effort at every considered concentration step. Since we are focusing on the whole range and a complete picture of the magnetic phase diagram, a detailed analysis of $x = 0.5$ GCMO is not included here.

Adding then more Ca does not change the qualitative picture. The FM order remains still the lowest magnetic ground state structure and the corresponding Curie temperatures are still high (> 80 K) (Fig. 1). However, the total energy difference to the A-AFM order is strongly reduced and at $x = 3/4$, the ferrimagnetic (FiM) order (Fig. 1) starts to compete for the lowest total energy. Here, J_x and J_z are equivalent, while the AFM coupling J_{xz} increases (Fig. 5).

C. Electron doping: $7/8 < x < 1$

The last doping regime represents essentially CaMnO_3 doped with few percent Gd ions adding excess electrons from Gd^{3+} . Therein, the A-AFM overcomes the ferromagnetic order (Fig. 6) because the strength of the magnetic coupling decreases and all three exchange parameters are of a similar magnitude, $J_x = 1.20$ meV, $J_z = 0.70$ meV, and $J_{xz} = -0.47$ meV (Fig. 5). But this latter energetic competition reduces also the total energy of other magnetic structures and makes them more likely. The lowest energy difference is realized by the FiM state (Fig. 6a) but also G-AFM and C-AFM show very low energy differences and might become more relevant. In particular the C-type AFM order was also assumed for $x = 0.8$ by Beiranvand *et al.* [16] but remains at $x = 7/8$ in our calculation still 11 meV higher in energy than the A-AFM.

This variation of potential antiferromagnetic structures offers a large playground for the study of basic principles in magnetic coupling and the resulting ground states. Hence, the electron doping concentration range $7/8 < x < 1$ is, in particular, scientifically interesting, because the experimental results vary a lot: Beiranvand *et al.* [16] did not detect an CO state for $x > 0.7$, but Khan *et al.* [61] found that it should coexist with OO simultaneously at $x = 0.85$ and be even very robust against external influence, since the application of a magnetic

field up to 15 T between 5 K to 300 K did not annihilate the charge ordering. In addition, colossal magneto resistance was detected at $0.8 < x < 0.9$ and $T = 10$ K, in the boundary between the CO-AFM insulating state and the cluster-glass (CG) state [16]. The latter was explained by the simultaneous existence of FM metallicity and an AFM insulating state [62].

IV. SUMMARY

We investigated theoretically the magnetic phase diagram of the whole GCMO series for the first time and observed a good qualitative agreement with the available experimental data [16]. We identified the different magnetic ground states being mainly a ferromagnetic coupling between the Mn magnetic moments with instabilities towards ferrimagnetic or A-type antiferromagnetic orientations. The calculated magnetic transition temperatures agree with the experimentally derived ones, although the discrepancies for concentrations $x > 60\%$ are larger than elsewhere. This might be connected with the unstable antiferromagnetic coupling between the Mn ions observed in the same concentration range. In summary, we obtained a rather good agreement between the numerical calculations based on the special quasi random structures simulating the miscibility of the GCMO series and the earlier experimental study of the whole concentration range [16]. Several interesting features has to remain open and interesting, e.g., non-collinear magnetism, or finite temperature charge ordering. Nevertheless, our study lays a basis for further experimental and theoretical studies of the solid solution rare earth manganites and in particular GCMO.

ACKNOWLEDGMENTS

This publication was funded by the German Research Foundation within the Collaborative Research Centre 762 (Projects No. A4 and No. B1) and the German Academic Research Council (Project number 57348127). The Jenny and Antti Wihuri Foundation is acknowledged for financial support. The computer resources of the Finnish IT Centre for Science (CSC), project No. 2000643, are acknowledged.

-
- [1] J. Mannhart and D. G. Schlom, *Science* **327**, 1607 (2010).
 - [2] S. Ismail-Beigi, F. J. Walker, A. S. Disa, K. M. Rabe, and C. H. Ahn, *Nat. Rev. Mater.* **2**, 17060 (2017).
 - [3] R. von Helmolt, J. Wecker, B. Holzapfel, L. Schultz, and K. Samwer, *Phys. Rev. Lett.* **71**, 2331 (1993).
 - [4] M. B. Salamon and M. Jaime, *Rev. Mod. Phys.* **73**, 583 (2001).
 - [5] T. Kimura, S. Ishihara, H. Shintani, T. Arima, K. T. Takahashi, K. Ishizaka, and Y. Tokura, *Phys. Rev. B* **68**, 060403 (2003).
 - [6] C. Zener, *Phys. Rev.* **82**, 403 (1951).
 - [7] P. W. Anderson and H. Hasegawa, *Phys. Rev.* **100**, 675 (1955).
 - [8] M. Fiebig, *J. Phys. D: Appl. Phys.* **38**, R123 (2005).
 - [9] E. O. Wollan and W. C. Koehler, *Phys. Rev.* **100**, 545 (1955).
 - [10] J. B. Goodenough, *Phys. Rev.* **100**, 564 (1955).

- [11] M. C. Langner, S. Zhou, G. Coslovich, Y.-D. Chuang, Y. Zhu, J. S. Robinson, W. F. Schlotter, J. J. Turner, M. P. Minitti, R. G. Moore, W. S. Lee, D. H. Lu, D. Doring, P. Denes, Y. Tomioka, Y. Tokura, R. A. Kaindl, and R. W. Schoenlein, *Phys. Rev. B* **92**, 155148 (2015).
- [12] K. Momma and F. Izumi, *J. Appl. Crystallogr.* **44**, 1272 (2011).
- [13] T. Kimura, G. Lawes, T. Goto, Y. Tokura, and A. P. Ramirez, *Phys. Rev. B* **71**, 224425 (2005).
- [14] Y. Yamasaki, H. Sagayama, N. Abe, T. Arima, K. Sasai, M. Matsuura, K. Hirota, D. Okuyama, Y. Noda, and Y. Tokura, *Phys. Rev. Lett.* **101**, 097204 (2008).
- [15] A. Pimenov, A. A. Mukhin, V. Y. Ivanov, V. D. Travkin, A. M. Balbashov, and A. Loidl, *Nat. Phys.* **2**, 97 (2006).
- [16] A. Beiranvand, J. Tikkanen, H. Huhtinen, and P. Paturi, *J. Alloys Comp.* **720**, 126 (2017).
- [17] J. M. Cadogan, D. H. Ryan, M. Napoletano, P. Riani, and L. M. D. Cranswick, *J. Phys.: Condens. Matter* **21**, 124201 (2009).
- [18] A. Zunger, S.-H. Wei, L. G. Ferreira, and J. E. Bernard, *Phys. Rev. Lett.* **65**, 353 (1990).
- [19] R. Kováčik, S. S. Murthy, C. E. Quiroga, C. Ederer, and C. Franchini, *Phys. Rev. B* **93**, 075139 (2016).
- [20] W. S. Ferreira, E. Moreira, and N. F. Frazão, *Braz. J. Phys.* **48**, 126 (2018).
- [21] C. Xu, Y. Li, B. Xu, J. Íñiguez, W. Duan, and L. Bellaiche, *Adv. Funct. Mater.* **27**, 1604513 (2017).
- [22] D. Mekam, S. Kacimi, M. Djermouni, M. Azzouz, and A. Zaoui, *Results Phys.* **2**, 156 (2012).
- [23] H. R. Aliabad, Z. Barzanuni, S. R. Sani, I. Ahmad, S. Jalali-Asadabadi, H. Vaezi, and M. Dastras, *J. Alloys Comp.* **690**, 942 (2017).
- [24] N. S. Fedorova, Y. W. Windsor, C. Findler, M. Ramakrishnan, A. Bortis, L. Rettig, K. Shimamoto, E. M. Bothschafter, M. Porer, V. Esposito, Y. Hu, A. Alberca, T. Lippert, C. W. Schneider, U. Staub, and N. A. Spaldin, *ArXiv e-prints* (2018), provided by the SAO/NASA Astrophysics Data System, [arXiv:1805.02172](https://arxiv.org/abs/1805.02172).
- [25] S. Bhattacharjee, E. Bousquet, and P. Ghosez, *Phys. Rev. Lett.* **102**, 117602 (2009).
- [26] U. Aschauer and N. A. Spaldin, *Appl. Phys. Lett.* **109**, 031901 (2016).
- [27] U. Aschauer, R. Pfenninger, S. M. Selbach, T. Grande, and N. A. Spaldin, *Phys. Rev. B* **88**, 054111 (2013).
- [28] S. Keshavarz, Y. O. Kvashnin, D. C. M. Rodrigues, M. Pereiro, I. Di Marco, C. Autieri, L. Nordström, I. V. Solov'yev, B. Sanyal, and O. Eriksson, *Phys. Rev. B* **95**, 115120 (2017).
- [29] N. Bondarenko, Y. Kvashnin, J. Chico, A. Bergman, O. Eriksson, and N. V. Skorodumova, *Phys. Rev. B* **95**, 220401 (2017).
- [30] J. Klarbring and S. I. Simak, *Phys. Rev. B* **97**, 024108 (2018).
- [31] G. Kresse and D. Joubert, *Phys. Rev. B* **59**, 1758 (1999).
- [32] G. Kresse and J. Furthmüller, *Comp. Mater. Sci.* **6**, 15 (1996).
- [33] G. Kresse and J. Furthmüller, *Phys. Rev. B* **54**, 11169 (1996).
- [34] J. P. Perdew, K. Burke, and M. Ernzerhof, *Phys. Rev. Lett.* **77**, 3865 (1996).
- [35] J. P. Perdew and Y. Wang, *Phys. Rev. B* **45**, 13244 (1992).
- [36] J. P. Perdew and A. Zunger, *Phys. Rev. B* **23**, 5048 (1981).
- [37] S. L. Dudarev, G. A. Botton, S. Y. Savrasov, C. J. Humphreys, and A. P. Sutton, *Phys. Rev. B* **57**, 1505 (1998).
- [38] See Supplemental Material at [URL will be inserted by publisher] for details about the computational setup, the validation of the choice of exchange-correlation functionals, and the special quasi random structures.
- [39] T. Mori, N. Kamegashira, K. Aoki, T. Shishido, and T. Fukuda, *Mater. Lett.* **54**, 238 (2002).
- [40] Neetika, A. Das, I. Dhiman, A. K. Nigam, A. K. Yadav, D. Bhattacharyya, and S. S. Meena, *J. Appl. Phys.* **112**, 123913 (2012).
- [41] W. H. Baur, *Acta Crystallogr. B* **30**, 1195 (1974).
- [42] K. Robinson, G. V. Gibbs, and P. H. Ribbe, *Science* **172**, 567 (1971).
- [43] X. L. Wang, D. Li, T. Y. Cui, P. Kharel, W. Liu, and Z. D. Zhang, *J. Appl. Phys.* **107**, 09B510 (2010).
- [44] P. Negi, G. Dixit, H. M. Agrawal, and R. C. Srivastava, *J. Supercond. Nov. Magn.* **26**, 1611 (2013).
- [45] N. N. Loshkareva, L. V. Nomerovannaya, E. V. Mostovshchikova, A. A. Makhnev, Y. P. Sukhorukov, N. I. Solin, T. I. Arbuzova, S. V. Naumov, N. V. Kostromitina, A. M. Balbashov, and L. N. Rybina, *Phys. Rev. B* **70**, 224406 (2004).
- [46] J. Hemberger, S. Lobina, H.-A. Krug von Nidda, N. Tristan, V. Y. Ivanov, A. A. Mukhin, A. M. Balbashov, and A. Loidl, *Phys. Rev. B* **70**, 024414 (2004).
- [47] G. Fischer, M. Däne, A. Ernst, P. Bruno, M. Lüders, Z. Szotek, W. Temmerman, and W. Hergert, *Phys. Rev. B* **80**, 014408 (2009).
- [48] Z. Zeng, M. Greenblatt, and M. Croft, *Phys. Rev. B* **59**, 8784 (1999).
- [49] A. van de Walle, P. Tiwary, M. de Jong, D. Olmsted, M. Asta, A. Dick, D. Shin, Y. Wang, L.-Q. Chen, and Z.-K. Liu, *Calphad* **42**, 13 (2013).
- [50] R. D. Shannon, *Acta Crystallogr. A* **32**, 751 (1976).
- [51] R. Korotana, G. Mallia, Z. Gercsi, L. Liborio, and N. M. Harrison, *Phys. Rev. B* **89**, 205110 (2014).
- [52] G. J. Snyder, C. H. Booth, F. Bridges, R. Hiskes, S. DiCarolis, M. R. Beasley, and T. H. Geballe, *Phys. Rev. B* **55**, 6453 (1997).
- [53] O. Pena, M. Bahout, K. Ghanimi, P. Duran, D. Gutierrez, and C. Moure, *J. Mater. Chem.* **12**, 2480 (2002).
- [54] O. Peña, Y. Ma, M. Guilloux-Viry, and C. Moure, *Appl. Surf. Sci.* **254**, 339 (2007), proceedings of the 13th International Conference on Solid Films and Surfaces.
- [55] M. Pełkala and V. Drozd, *J. Alloys Comp.* **437**, 12 (2007).
- [56] M. Hoffmann, V. S. Borisov, S. Ostanin, I. Mertig, W. Hergert, and A. Ernst, *Phys. Rev. B* **92**, 094427 (2015).
- [57] M. Hoffmann, V. Antonov, L. Bekenov, K. Kokko, W. J. Hergert, and A. Ernst, *J. Phys.: Condens. Matter* **30**, 305801 (2018).
- [58] P. Schiffer, A. P. Ramirez, W. Bao, and S.-W. Cheong, *Phys. Rev. Lett.* **75**, 3336 (1995).
- [59] A. Daoud-Aladine, J. Rodríguez-Carvajal, L. Pinsard-Gaudart, M. T. Fernández-Díaz, and A. Revcolevschi, *Phys. Rev. Lett.* **89**, 097205 (2002).
- [60] D. J. García, K. Hallberg, C. D. Batista, M. Avignon, and B. Alascio, *Phys. Rev. Lett.* **85**, 3720 (2000).
- [61] M. H. Khan and S. Pal, *Phys. Letters A* **379**, 401 (2015).

- [62] C. Martin, A. Maignan, M. Hervieu, B. Raveau, Z. Jirák, M. M. Savosta, A. Kurbakov, V. Trounov, G. André, and F. Bourée, *Phys. Rev. B* **62**, 6442 (2000).